



Nanoscale

**Trace Metals Dramatically Boost Oxygen Electrocatalysis of  
N-doped Coal-derived Carbon for Zinc-air Battery**

Journal:	<i>Nanoscale</i>
Manuscript ID	Draft
Article Type:	Paper
Date Submitted by the Author:	n/a
Complete List of Authors:	Liu, Huimin; University of Science and Technology Liaoning Huang, Xinning; University of Science and Technology Liaoning Lu, Zhenjie; University of Science and Technology Liaoning Wang, Tao; Institute of Applied Chemistry, Zhu, Yaming; University of Science and Technology Liaoning Cheng, Junxia; University of Science and Technology Liaoning Wang, Yue; University of Science and Technology Liaoning Wu, Dongling; Institute of Applied Chemistry, Xinjiang University Sun, Zhenyu; Beijing University of Chemical Technology College of Chemical Engineering, Chen, Xingxing; University of Science and Technology Liaoning,

SCHOLARONE™  
Manuscripts



Beijing University of Chemical Technology |100029 Beijing| China

To the Editor  
Nanoscale

*College of Chemical Engineering*

**Prof. Dr. Zhenyu Sun**

Chemical Engineering Building A501

Beijing Chaoyang District North Third Ring Road 15

[sunzy@mail.buct.edu.cn](mailto:sunzy@mail.buct.edu.cn)

[nanocarbon.cn](http://nanocarbon.cn)

23.12.2019

Enclosed please find our manuscript entitled “*Trace metals dramatically boost oxygen electrocatalysis of N-doped coal-derived carbon for zinc-air battery*” by Huimin Liu, Xinning Huang, Zhenjie Lu, Tao Wang, Yaming Zhu, Junxia Cheng, Yue Wang, Dongling Wu,<sup>\*</sup>, Zhenyu Sun,<sup>\*</sup> and Xingxing Chen, which we would like to submit for publication in *Nanoscale*.

Metal-air batteries possess very high theoretical energy densities but their rechargeability is still a challenge due to lack of efficient bifunctional catalysts for reversible oxygen electrodes. It is of paramount importance that bifunctional ORR/OER catalysts are not only efficient but also that they can be produced cheaply from abundant resources in the interest of sustainability, and potential for large-scale use. Coal is an attractive material with low cost and earth abundance that can be directly converted to useful electrocatalysts without the need for costly pre-refining treatment. However, the role of different trace metal elements in pristine coal on the performance of the catalysts still remains unclear. Herein, we make a systematic study on how different trace metal elements may boost oxygen electrocatalysis of coal-derived ORR/OER catalysts in alkaline solution. More importantly, we construct a rechargeable Zn-air battery, which shows excellent stability and can power a green LED bulb for more than 80 h, clearly underlining the robustness of the developed catalysts.

We declare that this manuscript has not been published and it is not under consideration for publication elsewhere. We are confident that this study will be highly interesting for scientists in the field of oxygen electrocatalysis. We are looking forward to hopefully positive referee comments.

Yours sincerely,

Zhenyu Sun

Professor, Dr.

College of Chemical Engineering

Beijing University of Chemical Technology

## Trace Metals Dramatically Boost Oxygen Electrocatalysis of N-doped Coal-derived Carbon for Zinc-air Battery

Huimin Liu<sup>a</sup>, Xinning Huang<sup>b</sup>, Zhenjie Lu<sup>a</sup>, Tao Wang<sup>c</sup>, Yaming Zhu<sup>a</sup>, Junxia Cheng<sup>a</sup>, Yue Wang<sup>a</sup>, Dongling Wu<sup>c,\*</sup>, Zhenyu Sun<sup>d,\*</sup> and Xingxing Chen<sup>a,\*</sup>

<sup>a</sup> *Research Group of Functional Materials for Electrochemical Energy Conversion, School of Chemical Engineering, University of Science and Technology Liaoning, Qianshan Middle Road 185, 114051 Anshan, P. R. China*

<sup>b</sup> *Engineering Training Center, University of Science and Technology Liaoning, Qianshan Road 185, 114051 Anshan, P. R. China*

<sup>c</sup> *Key Laboratory of Energy Materials Chemistry, Institute of Applied Chemistry, Xinjiang University, Shengli Road 14, 830046 Urumqi, P. R. China*

<sup>d</sup> *State Key Laboratory of Organic-Inorganic Composites, College of Chemical Engineering, Beijing University of Chemical Technology, Beijing 100029, P. R. China*

\* *Corresponding authors. E-mail: xingchenstar79@163.com (X. X. Chen), wudl@xju.edu.cn (D. L. Wu), sunzy@mail.buct.edu.cn (Z. Y. Sun)*

## Abstract

The commercialization of metal-air batteries requires efficient, low-cost, and stable bifunctional electrocatalysts for reversible electrocatalysis of the oxygen reduction reaction (ORR) and the oxygen evolution reaction (OER). The modification of natural coal by heteroatoms such as N and S, or metal oxide species, has been demonstrated to form very promising electrocatalysts for the ORR and OER. However, it remains elusive and underexplored on how the impurity elements in coal may impact the electrocatalytic properties of coal-derived catalysts. Herein, we explore the influence of the presence of various trace metals that are notable impurities in coal, including Al, Si, Ca, K, Fe, Mg, Co, Mn, Ni, and Cu, on the electrochemical performance of the prepared catalysts. The constructed Zn-air batteries are further shown to be able to power green LED lights for more than 80 h. The charge-discharge polarization curves exhibited excellent and durable rechargeability over 500 (*ca.* 84 h) continuous cycles. The promotional effect of the trace elements is believed to accrue from a combination of electronic structure modification of the active sites, enhancement of the active site density, and formation of a conductive 3-dimensional hierarchical network of carbon nanotubes.

## Keywords

Oxygen reduction reaction (ORR), Oxygen evolution reaction (OER), Coal, Carbon Nanotubes (CNTs), Trace metals

## 1. Introduction

A looming energy crisis and environmental pollution are major problems facing humanity today, consequently, the development and use of non-polluting and sustainable renewable energies has received extensive attention. Achieving efficient, economical, and environmentally friendly energy conversion and storage systems is inevitably urgent for both current and future development [1-4]. The oxygen reduction reaction (ORR) and the oxygen evolution reaction (OER) are a pair of reversible electrochemical reactions involved in electrochemical energy conversion devices such as fuel cells and metal air batteries, among others, that are key to future green energy systems. However, slow kinetics and frustratingly poor reversibility are key hindrances that limit the energy efficiency of metal-air batteries and regenerative fuel cell systems [5,6]. The best catalysts for ORR invariably consist of Pt, however, the OER activity of Pt is unsatisfactorily poor [7,8], meanwhile, oxides of Ru and Ir are benchmark OER catalysts but exhibit dismal ORR activity [8,9]. A commonly adopted strategy for designing effective bifunctional ORR/OER catalysts involves the integration of individually excellent ORR and OER catalysts into a composite material embodying both functions. To this end, alloys of Pt, Ir, and Ru have been widely evaluated as bifunctional oxygen electrodes and they represent the archetypical benchmark, especially when used under acidic conditions. However, wide-scale technological application of such materials is evidently prohibitive due to their high cost and scarcity [10-13]. As such, the pursuit of non-

precious and effective bifunctional ORR/OER electrocatalysts is a research undertaking of topical importance.

Some of the most promising potential replacements that have been developed in recent years include heteroatom (e.g. N, S, P, B and Si) and single metallic atom (e.g. Fe, Mn and Co)-doped carbon materials <sup>[14-19]</sup>, among others. Among the carbon-based materials, coal has the advantages of low cost and abundant availability. Nagai et al. reported the use of coal as a raw material to prepare electrocatalysts for the ORR in acidic media <sup>[20-23]</sup>. We have also reported the feasibility to convert coal into promising ORR, OER and bifunctional ORR/OER electrocatalysts in alkaline media <sup>[11,24-26]</sup>. It was previously demonstrated that coal can be directly modified into ORR, OER or bifunctional ORR/OER active catalysts without prior purification. However, natural coal has a very complex composition, consisting of C, H, O, N and S together with other inorganic elements (e.g. Si, Fe, Mn, Al and Mg) <sup>[20,24]</sup>. The electrocatalytic properties of carbon can be tremendously altered by the mere presence of traces of particular elements, either individually or through their interaction with other elements present in the coal. It would thus be prudent to understand how the various impurities in coal impact its electrocatalytic properties.

Here, we study for the first time the influence of traces of Fe, Al, Ca, K, Co, Si, Mg, Cu, Ni, and Mn, the notable impurity elements in coal, on its electrocatalytic ORR and OER performance. To achieve this, natural coal was first purified through treatment with hydrochloric acid and hydrofluoric acid to remove

inorganic impurities. The purified coal was then impregnated with 1 wt% of precursors of the elements of interest and subsequently treated in a stream of ammonia at 1050 °C. Electrochemical ORR and OER studies of the investigated elements show that traces of Fe, Al, Ca, K, and Co promote electrocatalysis of the ORR and OER. Promotion of the ORR and OER by Fe and Co is consistent with those results reported over M-N/C type catalysts for ORR, as well as metal oxides supported on, or embedded inside carbon structures <sup>[13,14]</sup>. The promotional effect of Al, Ca and K is quite interesting. So far, there are five possible hypotheses that could account for this observation. Firstly, we observed the formation of carbon nanotubes (CNTs) when purified coal impregnated with Fe, Al, Ca, K, and Co was treated in ammonia at 1050 °C. This observation is not surprising in the case of the Fe and Co containing samples, as they are commonly used catalysts for the growth of CNTs. In this case, the carbon precursors for growth of the CNTs are expected to be the volatile organic components in the coal. It was also reported that the CNTs were successfully grown on a pyrolytic graphite paper tape using  $\text{CaSiO}_3$  as the catalyst. The growth of the CNTs was ascribed to the critical melting temperature of  $\text{CaSiO}_3$  and silicate that seemed to play an important role similar to transition metals <sup>[27]</sup>. But the growth of CNTs from purified coal samples impregnated with Al, and K after treatment in ammonia at 1050 °C was surprising as these elements are not known to catalyze the growth of CNTs. Although it is possible that the purified coal could still have contained residual

transition metallic species that facilitated growth of the CNTs in the case of the Al, Ca, and K containing samples, it is evident to infer that growth of the CNTs must have contributed to enhancement of the ORR and OER activity. In addition, much as Al, Ca and K may not directly function as catalysts to grow the CNTs, they are well-known reduction agents [28-30], and could possibly facilitate reduction of the real trace catalyst prior to growth of CNTs. Secondly, in the case of growth of the CNTs, Al, Ca and K, may contribute to enhancement of the ORR and OER activity of the catalyst through electronic modification of the active sites, either when encapsulated inside the CNTs, or in tandem through direct interaction with the active sites. Thirdly, transition metals and Ca have been reported to favor the reactivity of coal pyrolysis and the decomposition of unstable volatiles [11,26,31]. The existence of those trace metals would lead to surface defects such as multiple atom vacancies arising from structural reconstruction of the coal-based pyrolyzed carbon by the removal of heteroatoms (e.g. S and N). Meanwhile, a more porous structure with higher surface area is expected to be formed. Fourth, the melting points of the used precursors  $\text{AlCl}_3$  (192.6 °C),  $\text{KNO}_3$  (334 °C), and  $\text{CaCl}_2$  (772 °C) are all far below the employed thermal temperature of 1050 °C. Thus, the infusion of these species through the carbon network under these pyrolysis conditions is not only likely to induce the formation of a porous structures but also uniquely tailor the properties of the final catalyst. Finally, despite the rather low solubility product of  $\text{Ca(OH)}_2$ , Al, K and Ca are all expected to dissolve as aluminates

$\text{Al}(\text{OH})_4^-$ , KOH and  $\text{Ca}(\text{OH})_2$  through reaction with the electrolyte, thereby increasing the catalyst porosity and active site density due to the accompanying surface area enhancement.

## 2. Results and discussion

The original brown coal (OC) was first crushed by ball milling followed by drying in an oven at 378 K for 4 h to obtain air-dried coal. After acid pretreatment with HCl and HF, the purified coal (PC) was obtained. It was then added to different trace element precursors ( $\text{FeCl}_3 \cdot 6\text{H}_2\text{O}$ ,  $\text{AlCl}_3$ ,  $\text{CaCl}_2$ ,  $\text{KNO}_3$ ,  $\text{Co}(\text{NO}_3)_2 \cdot 6\text{H}_2\text{O}$ ,  $\text{SiCl}_4$ ,  $\text{MgCl}_2$ ,  $\text{C}_4\text{H}_6\text{CuO}_4 \cdot \text{H}_2\text{O}$ ,  $\text{NiN}_2\text{O}_6 \cdot 6\text{H}_2\text{O}$ , or  $\text{C}_4\text{H}_6\text{MnO}_4 \cdot 4\text{H}_2\text{O}$ ) in an ethanol solution. The trace element (Fe, Al, Ca, K, Co, Si, Mg, Cu, Ni, or Mn) to PC weight ratio was 1 wt%, respectively. After thorough mixing of the suspension, it was dried at room temperature overnight. The samples were thermally treated in a stream of  $\text{NH}_3$  and Ar (1:9 volume ratio) at 1050 °C for 2 h in a chemical vapor deposition (CVD) reactor. The prepared catalysts are denoted as NPCC (N-doped purified coal-derived carbon), without the addition of trace elements, as the reference sample, Fe-NPCC, Al-NPCC, Ca-NPCC, K-NPCC, Co-NPCC, Si-NPCC, Mg-NPCC, Cu-NPCC, Ni-NPCC, and Mn-NPCC (see Supporting information for more experimental details).

The composition of C, H, N, S, O, and other trace elements, in OC, PC, and NPCC were characterized by elemental analysis, as summarized in Table 1. The content of impurities was drastically decreased after the acid purification

steps, and even decreased after thermal treatment. Decrease of the H and O contents after thermal treatment was due to the release of unstable volatile components<sup>[11]</sup>. The N content clearly increased after thermal treatment of the samples under ammonia at 1050 °C, demonstrating successful introduction of nitrogen in the carbon. It seems that the acid pre-purification processes did not facilitate the removal of S, however, a significant decrease of the sulphur content was observed after the thermal treatment step, suggesting the removal of unstable sulphur components.

**Table 1.** Elemental analysis of OC, PC, and NPCC.

Sample	C%	H%	N%	S%	O%	Others%
OC	57.20	3.69	1.02	0.13	25.39	12.57
PC	65.82	3.26	2.94	0.11	23.14	4.73
NPCC	83.68	0.78	5.31	0.06	8.73	1.44

The morphology of the PC, NPCC, and NPCC incorporated with trace elements (Fe, Al, Ca, K, Co) was studied by scanning electron microscopy (SEM) (Figure 1). Interestingly, although no extra carbon source was introduced during the thermal treatment, bamboo-like CNTs ranging from a few tens to hundreds of nanometers in diameter were clearly observed when the above trace metal elements were introduced into PC before thermal treatment. It is believed that the PC itself was the carbon source, and the introduced trace elements were

the possible active domains for catalyzing or promoting the growth of CNTs from volatile organic compounds arising from decomposition of the coal. It is known that transition metals such as Fe, Co, Ni promote CNT growth<sup>[32-34]</sup>. Interestingly, here we found that Al, Ca, and K can also facilitate the growth of CNTs. It is well known that Al, Ca, and K are reduction agents, which may have an effect on reducing real trace metal catalysts left in the PC residual during thermal treatment, thus promoting the growth of CNTs. On the contrary, no growth of CNTs was discerned in PC and NPCC samples (Figure 1a and 1b). Note that the formation of CNTs facilitated creation of a 3-dimensional hierarchical structure in the PC-derived carbon with large active surface areas, thus contributing to the improvement of electrocatalytic performance.

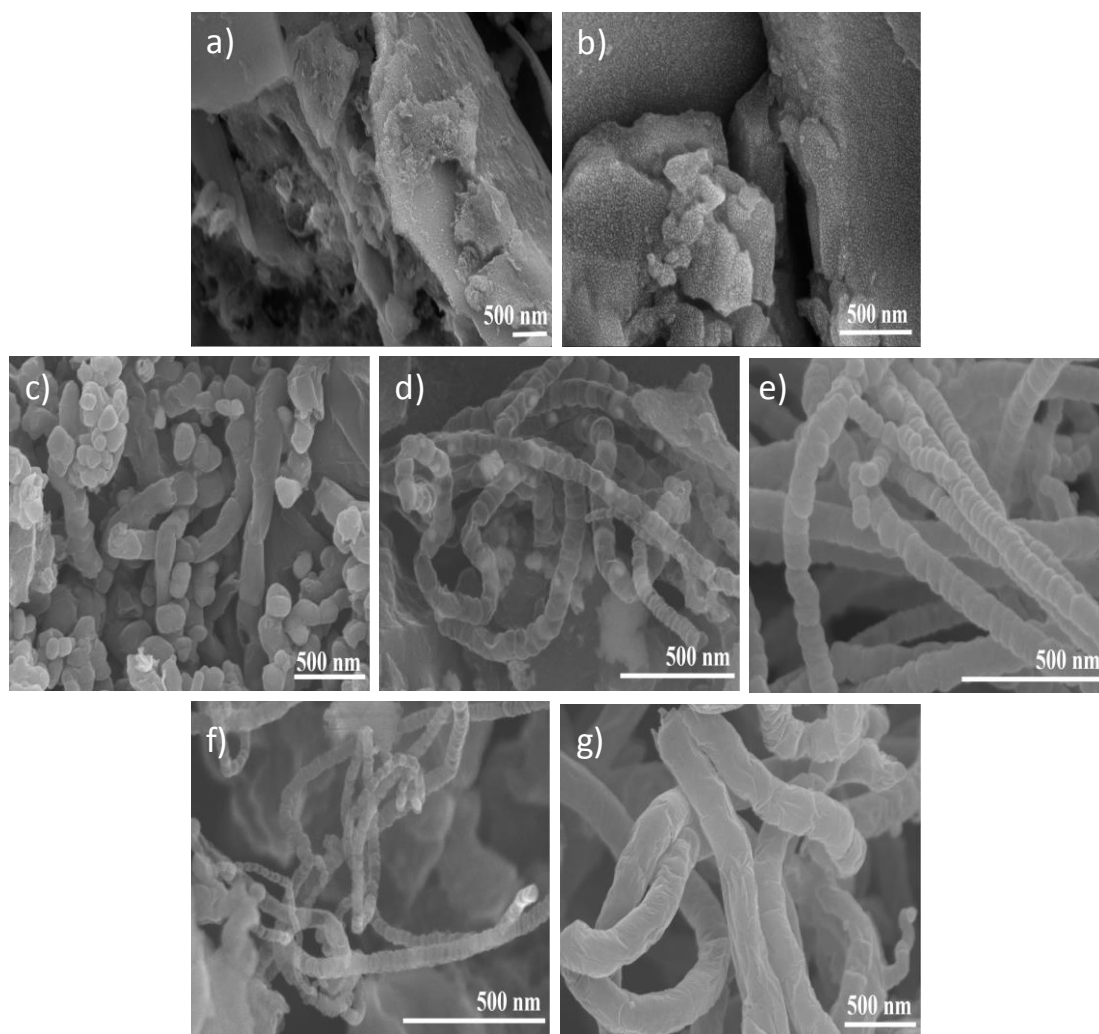


**Figure 1.** SEM images of a) PC, b) NPCC, c) Fe-NPCC, d) Al-NPCC, e) Ca-NPCC, f) K-NPCC, and g) Co-NPCC.

Transmission electron microscopy (TEM) was further employed to examine the microstructure of the prepared samples, as shown in Figure 2. In all trace metal containing NPCC samples, dark spots were seen, which are typically embedded in a carbon network, indicating the existence of metal nanoparticles (Figure 2c-h). CNTs were also identified, consistent with SEM observation. Figure 2a and 2b show the TEM images of PC and NPCC, displaying the co-existence of both the graphitic and amorphous carbon structures. However, no

metals could be discerned in these two samples, demonstrating that most of the trace elements in the pristine coal were washed away during acid pretreatment.

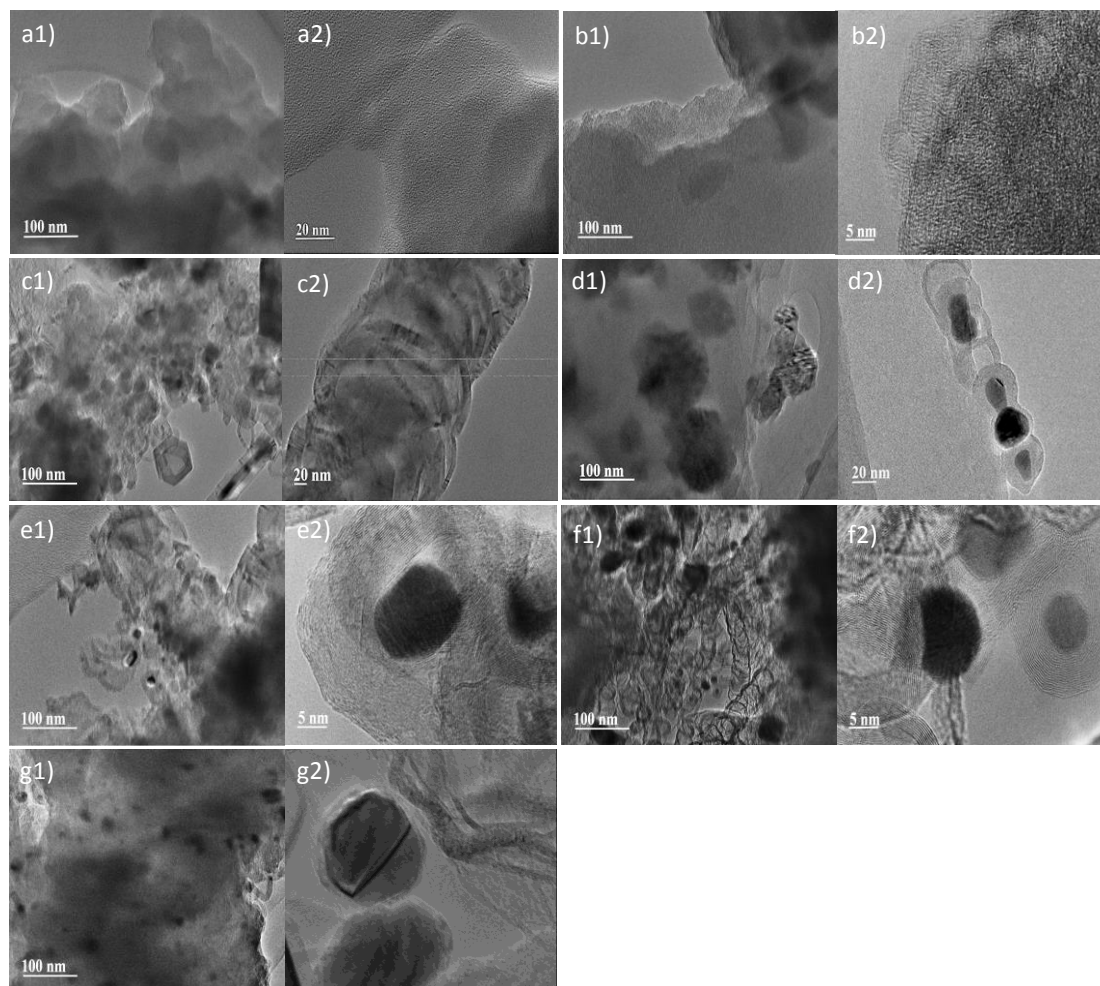


**Figure 2.** TEM images of a) PC, b) NPCC, c) Fe-NPCC, d) Al-NPCC, e) Ca-NPCC, f) K-NPCC, and g) Co-NPCC.

Raman spectroscopy provides insight into the graphitization degree of the prepared carbon materials (Figure 3a). The two strong peaks at 1342 (D band) and 1586  $\text{cm}^{-1}$  (G band) correspond to disordered  $sp^3$  structures and  $sp^2$ -hybridized graphitic carbon, respectively<sup>[35]</sup>. Generally, the higher the intensity

ratio of the D-to the G-band ( $I_D / I_G$ ), the higher the defect degree and content of disordered carbon in the carbon materials [36]. The  $I_D / I_G$  value of PC (0.73) was considerably much smaller than that of the other samples (NPCC: 1.25; Fe-NPCC: 1.00; Al-NPCC: 1.14; Ca-NPCC: 1.10; K-NPCC: 1.10; Co-NPCC: 1.06). This indicates introduction of defects when PC was pyrolyzed in ammonia at 1050 °C. Such observation is in accordance with previous results that incorporation of nitrogen in carbon can occupy its lattice positions, thus leading to increase of disorder in the carbon structure [11,37]. Upon introduction of trace metals prior to the pyrolysis, the intensity ratio of D-to-G-bands slightly decreased. This is due to the decomposition of unstable volatiles generated from the PC carbon matrix catalyzed by the trace metals during the thermal treatment [25,38]. However, no clear peak shifts or line broadening of the G- and D-bands was observed, indicating that the properties of the carbon structure remained apparently unchanged after the doping [39]. The 2D-band ( $2680\text{ cm}^{-1}$ ) and (D + G)-band ( $2920\text{ cm}^{-1}$ ), which originate from the crystalline graphitic domains and structural disorder or defects, respectively, could be seen for the trace metal-containing NPCC samples. This suggests that stronger structural distortion of the aromatic graphitic carbon domains took place when trace metals were introduced into NPCC [25,26,40,41].

The XRD patterns of the PC and NPCC-based samples are presented in Figure 3b. Both PC and NPCC samples have broad reflections at *ca.*  $2\theta$  of 18 to 29°. In the case of PC, this was because of presence of carbon with a predominantly

amorphous structure, while for the NPCC sample, the ordered arrangement of graphene stacks was distorted by the dopant nitrogen atoms after thermal treatment in  $\text{NH}_3$ . For the trace metal-containing NPCC samples, dominant reflections with a clear peak at  $\text{ca. } 26^\circ$  were observed. This is attributed to the formation of a higher proportion of graphite-like structures with the trace metals, facilitating catalytic decomposition of the unstable volatile carbon-rich organic components [38]. The presence of a pronounced peak at  $\text{ca. } 44^\circ$  is indicative of the presence domains of ordered graphene sheets [20,32,42]. Unfortunately, the presence of the trace metals could not be revealed by XRD at such low concentrations.

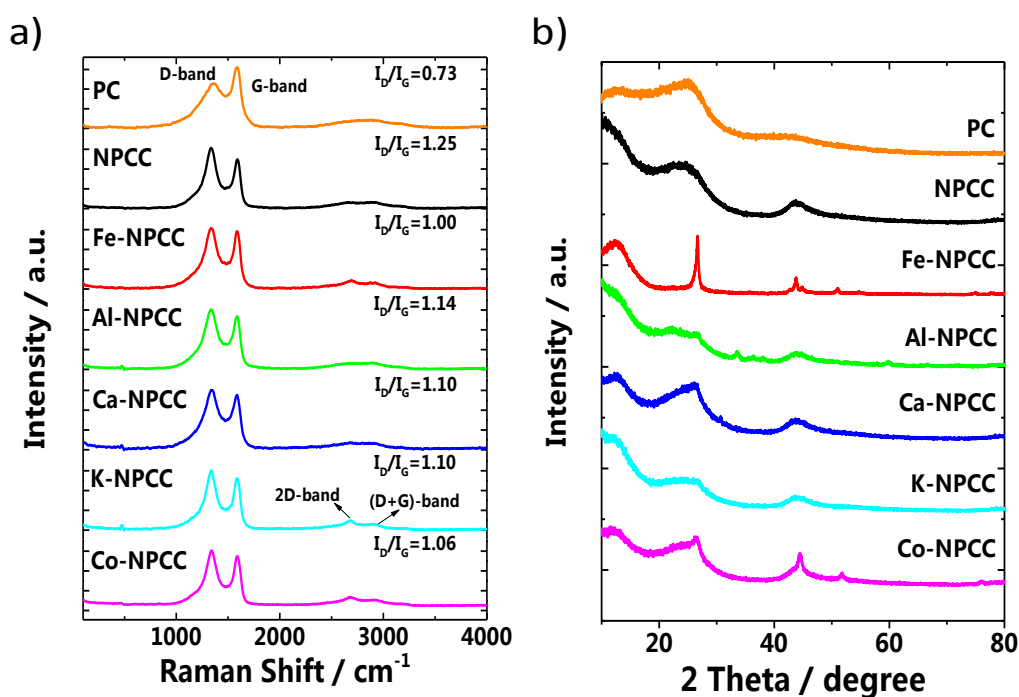


**Figure 3.** a) Raman spectra and b) XRD patterns of PC, NPCC, Fe-NPCC, Al-NPCC, Ca-NPCC, K-NPCC, and Co-NPCC.

XPS was employed to investigate the surface chemical compositions and oxidation states of the samples. Figure 4a shows the wide-survey XPS spectra of the PC, NPCC, and metal-containing NPCC samples, which confirm the existence of C, O and N atoms in all cases. However, the presence of the metals cannot be identified at this low-resolution probably owing to their low concentrations. The O 1s spectra were deconvoluted into three different contributions at 530.8, 531.8, and 532.9 eV (Figure 4b). The peak centered at 530.8 eV is due to anionic oxygen associated with oxide species ( $O^{2-}$ ) of metals, such as Fe, Al, Ca, K, and Co. The peaks at 531.8 and 532.9 eV are related to C=O and C-O functional groups on the carbon surface, respectively [9]. Their relative distributions are summarized in Table 2 and Figure 4e. The total oxygen content was drastically decreased after high-temperature treatment. This is mainly attributed to its loss as part of the high-temperature decomposition products, and the exchange with nitrogen atoms during N-doping treatment [24]. Among the three oxygen species, the relative contribution of  $O^{2-}$  groups in the NPCC-based samples generally increased after the thermal treatment, indicating the formation of metal oxides. Three nitrogen species, namely, pyridinic-N, pyrrolic-N, and graphitic-N were deconvoluted from the high-resolution N 1s spectra, as shown in Figure 4c. As summarized in Table 2 and Figure 4f, the total nitrogen content increased after thermal treatment in  $NH_3$ . Among the three species, the content of pyridinic-N significantly increased, and the content of graphitic-N also increased in general after the high-temperature

treatment, which has been reported to promote the oxygen reduction <sup>[7,8]</sup>. The N 1s XPS spectrum of NPCC was deconvoluted into three peaks at 398.5, 400.5, and 401.5 eV, corresponding to pyridinic-N, pyrrolic-N, and graphitic-N, respectively. However, an apparent peak shift in the characteristic binding energy of pyridinic-N was observed in the NPCC samples containing trace metals, which could arise from the formation of metal-N-C moieties. Figure 4d presents high-resolution Fe 2p, Al 2p, Ca 2p, K 2p and Co 2p XPS spectra of NPCC-based samples. The main signal of the Al 2p spectrum in Al-NPCC was at 73.8 eV, which is attributed to the presence of Al<sub>2</sub>O<sub>3</sub> <sup>[43]</sup>. The Ca 2p spectrum of Ca-NPCC consisted of two bands associated with Ca 2p<sub>3/2</sub> (347.4 eV) and Ca 2p<sub>1/2</sub> (350.9 eV) <sup>[44]</sup>. However, no clear characteristic 2p signals of Fe, K, and Co could be observed in the respective Fe-NPCC, K-NPCC, and Co-NPCC samples. Because XPS is a surface-sensitive technique with a maximum detection depth of ca. 10 nm on the sample surfaces <sup>[45]</sup>, the results imply that the surface concentration of the metals in these catalysts was too low to be detectable by XPS, or the metals were most likely encapsulated inside graphene layers as observed by TEM in our previous studies.

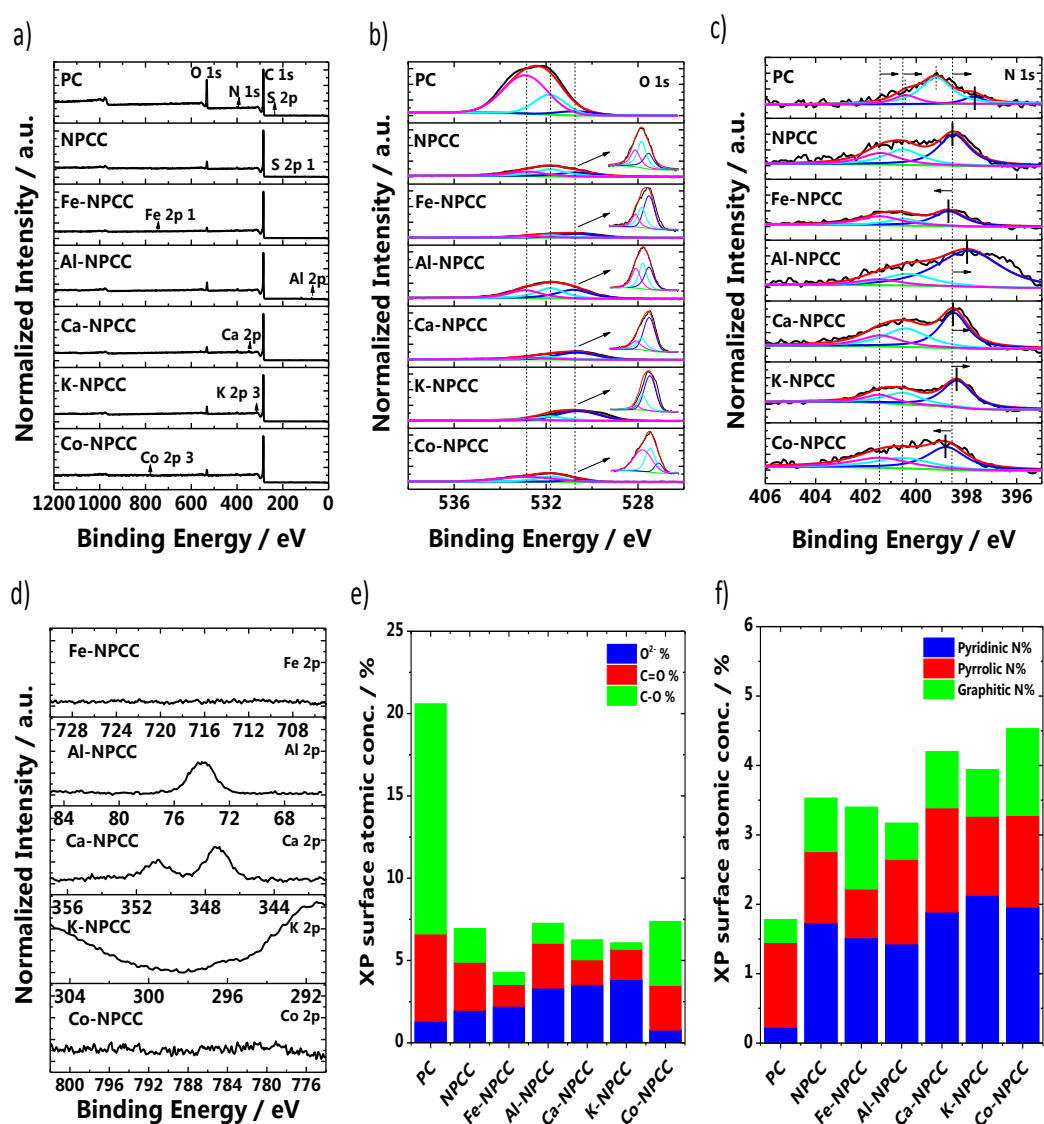


**Figure 4.** a) Wide-survey XPS spectra, b) O 1s, c) N 1s, and d) Fe 2p, Al 2p, Ca 2p, K 2p, and Co 2p XPS spectra of corresponding samples; and XPS-derived surface atomic concentrations of different e) oxygen groups and f) nitrogen groups for PC, NPCC, Fe-NPCC, Al-NPCC, Ca-NPCC, K-NPCC, and Co-NPCC.

**Table 2.** Total O and N concentrations, and the relative contributions of different nitrogen and oxygen groups obtained by deconvolution of the O 1s and N 1s XPS spectra.

Sample	O 1s				N 1s			
	Total O	O <sup>2-</sup>	C=O	C-O	Total	Pyridinic	Pyrrolic	Graphitic
	% <sup>[a]</sup>	% <sup>[b]</sup>	% <sup>[b]</sup>	% <sup>[b]</sup>	N% <sup>[a]</sup>	N% <sup>[b]</sup>	N% <sup>[b]</sup>	N% <sup>[b]</sup>
PC	20.59	6.4	25.7	67.9	1.78	12.6	68.8	18.6
NPCC	6.94	28.5	42.1	29.4	3.53	48.9	29.2	21.9
Fe-NPCC	4.28	52.2	30.8	17.0	3.4	44.7	20.7	34.6
Al-NPCC	7.26	45.9	37.4	16.7	3.17	45.2	38.5	16.3
Ca-NPCC	6.25	56.5	24.4	19.1	4.2	44.9	35.7	19.4
K-NPCC	6.07	63.4	30.3	6.3	3.94	53.9	29.0	17.1
Co-NPCC	7.37	10.8	36.9	52.3	4.53	43.2	29.0	27.8

<sup>[a]</sup> The concentration of total element O and N with the sample as the basis.

<sup>[b]</sup> The relative contribution of different nitrogen and oxygen groups obtained by deconvolution of the O1s and N 1s XPS spectra.

The electrocatalytic performance of the PC-derived catalysts towards the ORR was examined in 0.1 M NaOH saturated with O<sub>2</sub> (Figure 5, Figure S2 & S3). The important parameters including the onset potential, half-wave potential, and Tafel slope of different samples are investigated and summarized in Tables 3 and S2. Shown in Figure 5a and 5b are linear sweep voltammograms for the

ORR recorded at the RRDE disk, and corresponding potential-dependent current response for  $\text{H}_2\text{O}_2$  oxidation at the Pt-ring poised at a constant potential of 0.4 V (Ag/AgCl 3 M KCl), which can be a marker for the catalyst selectivity during the ORR. Among the prepared samples, the Ca-NPCC displayed the most positive onset potential (1.014 V) at a current density of  $-0.1 \text{ mA cm}^{-2}$ , followed by Fe-NPCC (0.990 V), Al-NPCC (0.973 V), K-NPCC (0.970 V), and Co-NPCC (0.968 V). All these catalysts are better than the metal-free N-doped catalyst NPCC with an onset potential of 0.928 V (Figure S4a). Ca-NPCC, Fe-NPCC, Al-NPCC, K-NPCC, and Co-NPCC also exhibited excellent half-wave potentials ( $E_{1/2}$ ) of 0.921, 0.921, 0.881, 0.865, and 0.870 V, respectively, remarkably higher than that for NPCC (0.811 V) (Figure S4b). Results for the electron transfer number per oxygen molecule ( $n$ ) for ORR determined from the RRDE data are presented in Figure 5c. Note that  $n$  is higher than 3 in the potential range of 0.2–0.8 V for all the samples. In particular,  $n$  is close to 4 for Ca-NPCC, Fe-NPCC, Al-NPCC, K-NPCC, and Co-NPCC, outperforming that of the catalysts incorporated with many other elements (e.g. Mg, Ni, Si, Mn, Cu) (Figure S3). The Tafel plots derived from Figure 5a are shown in Figure 5d. Ca-NPCC, Fe-NPCC, Al-NPCC, K-NPCC, and Co-NPCC all exhibited considerably smaller Tafel slopes of 53, 43, 57, 48, and 65 mV, respectively, in contrast to 85  $\text{mV dec}^{-1}$  for NPCC. This indicates that introduction of these trace metals significantly enhanced the ORR kinetics. For the samples with a Tafel slope close to 60  $\text{mV dec}^{-1}$ , the rate-determining step is likely the chemical step

following the fast one-electron transfer step. However, the Tafel slopes of the other NPCC samples are close to  $120 \text{ mV dec}^{-1}$ , indicating that the ORR mechanism involved a slow charge transfer step preceding a fast-chemical step. A Tafel slope between 60 and  $120 \text{ mV dec}^{-1}$  implies that the ORR process is governed by both mechanisms [26]. The addition of Mg, Mn, Ni, Cu and Si was found to be unable to improve the ORR performance of NPCC (Figure S3).

The long-term stability of ORR electrocatalysts is crucial for their practical application as cathode materials. Therefore, ORR durability tests for the three best catalysts (Ca-NPCC, Fe-NPCC and Al-NPCC) were performed galvanostatically at a constant current density of  $-1 \text{ mA cm}^{-2}$ . As displayed in Figure 5e, all the three catalysts showed very promising stability with the potential remained almost unchanged after 280 hours. The potential retention was 98%, 98%, and 93% for Ca-NPCC, Fe-NPCC, and Al-NPCC, respectively. The three samples were further exposed to methanol to evaluate their response to possible fuel crossover effects (Figure 5f). The presence of methanol is notoriously known to rapidly poison the ORR activity of Pt group metals due to strong adsorption of methanol oxidation products, or intermediates such as CO molecules that block ORR active sites. When methanol (3 M) was added to the electrolyte, the ORR currents for Ca-NPCC, Fe-NPCC, and Al-NPCC were unaffected, thus revealing their excellent tolerance to methanol crossover. Whereas the commercial reference catalyst Pt/C suffered from a sharp decrease in ORR current as a result of the oxidation of methanol on the catalyst

surface and possible formation of CO that blocks the ORR active sites <sup>[46]</sup>.

**Table 3.** The ORR performance of NPCC samples with the addition of different trace elements (Fe, Al, Ca, K, and Co).

Sample	$E_{\text{onset}}$	$E_{1/2}$	Tafel Slope	ET-Number
	(mV)	(mV)	(mV dec <sup>-1</sup> )	( <i>n</i> )
NPCC	0.928	0.811	85	3.66
Fe-NPCC	0.99	0.921	43	3.89
Al-NPCC	0.973	0.881	57	3.88
Ca-NPCC	1.014	0.928	53	3.78
K-NPCC	0.97	0.865	48	3.75
Co-NPCC	0.968	0.87	65	3.78

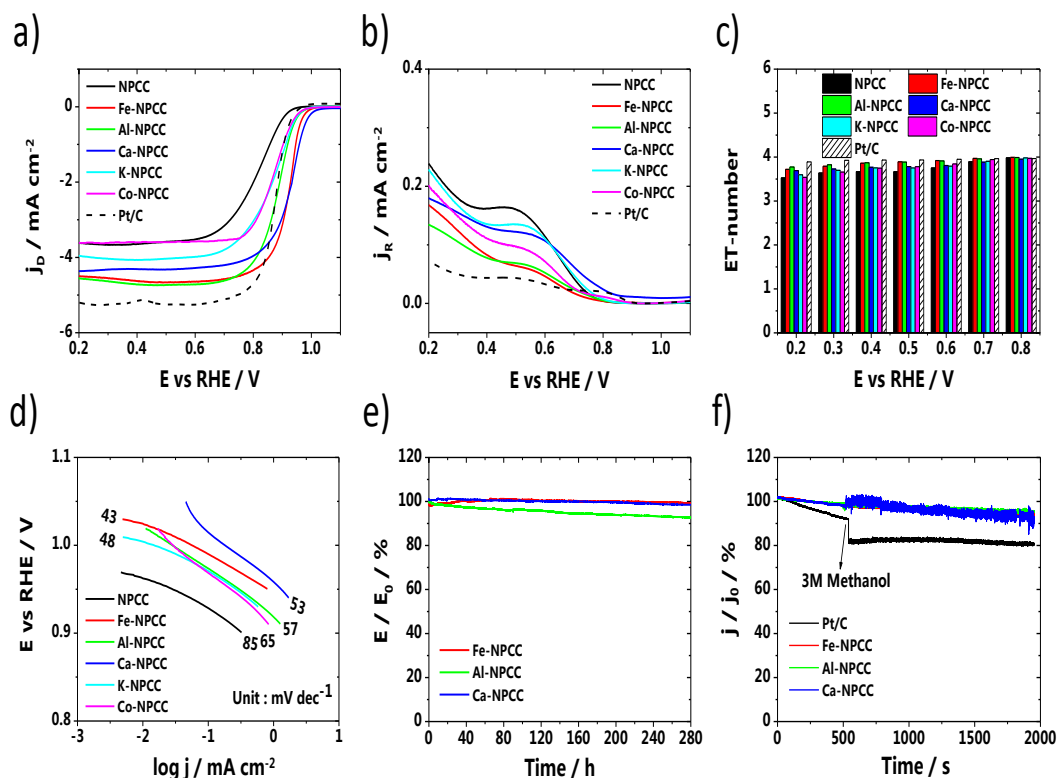


**Figure 5.** Linear sweep voltammetry (LSV) curves of the NPCC and metal (Fe, Al, Ca, K and Co)-doped NPCC samples during a) the ORR and b) H<sub>2</sub>O<sub>2</sub> production at 1600 rpm in O<sub>2</sub>-saturated 0.1 M NaOH solution with a scan rate of 5 mV s<sup>-1</sup>. c) Average electron transfer number at different potentials, d) Tafel plots derived from the ORR curves in a), and e) durability tests of Fe-NPCC, Al-NPCC, Ca-NPCC. f) Crossover effect measurements of Fe-NPCC, Al-NPCC, Ca-NPCC, and commercial Pt/C catalysts at an applied potential of -0.2 V.

We further explored the electrochemical performance of the prepared catalysts for the oxygen evolution reaction (OER). Linear sweep voltammograms were recorded between 1.0 and 2.0 V vs. RHE at a scan rate of 5 mV s<sup>-1</sup> with electrode rotation at 1600 rpm in 0.1 M NaOH. As shown in Figure 6a, S2 and S5, both Fe-NPCC and Al-NPCC exhibited higher current densities and smaller onset potentials than the other catalysts. The onset potential for Fe-NPCC and

Al-NPCC, defined as the potential corresponding to a current density of  $1 \text{ mA cm}^{-2}$ , were 1.40 and 1.34 V, respectively. The potentials at the current density of  $10 \text{ mA cm}^{-2}$ , a metric relevant to solar fuel synthesis [8], were 1.77 and 1.72 V, respectively, for Fe-NPCC and Al-NPCC, better than that for Pt/C (1.90 V) [47]. The Tafel plots for the OER derived from Figure 8a are shown in Figure 6b. A Tafel slope of  $\text{ca. } 60 \text{ mV dec}^{-1}$  usually suggests that a chemical step after the first electron transfer is rate limiting, while a Tafel slope close to  $40 \text{ mV dec}^{-1}$  means that the second electron transfer step of the OER determines the reaction rate [25]. We note that the Fe-NPCC and Al-NPCC had the smallest Tafel slopes of 36 and  $35 \text{ mV dec}^{-1}$ , respectively, demonstrating superior OER kinetics compared to the other electrocatalysts. We subsequently tested the OER stability of Fe-NPCC and Al-NPCC by continuously running CVs between 0.0 to 1.2 V vs. Ag/AgCl/3 M KCl in  $\text{O}_2$ -saturated 0.1 M NaOH. The LSV curves recorded before and after 1000 cycles of cyclic voltammograms for the two samples are presented in Figure 6c and 6d, respectively. Excellent preservation of the OER activity of the catalysts can be clearly observed. In the case of Al-NPCC, a slight but noticeable improvement of the OER performance was observed after the long-term CV experiment, probably due to morphological changes of the catalyst film or change in the surface properties such as gradual surface oxidation, leading to activation of more surface sites for the OER.

The bifunctionality of the catalysts for both ORR and OER were judged by the difference between the potential required for ORR at a current density of  $-1 \text{ mA}$

$\text{cm}^{-2}$  and the OER at a current density of  $10 \text{ mA cm}^{-2}$ . Fe-NPCC and Al-NPCC achieved a voltage difference of only 0.780 and 0.743 V, respectively, indicating a remarkable performance for a reversible oxygen electrode. Although Ca-NPCC showed excellent ORR performance, the catalyst presented rather dismal OER activity.

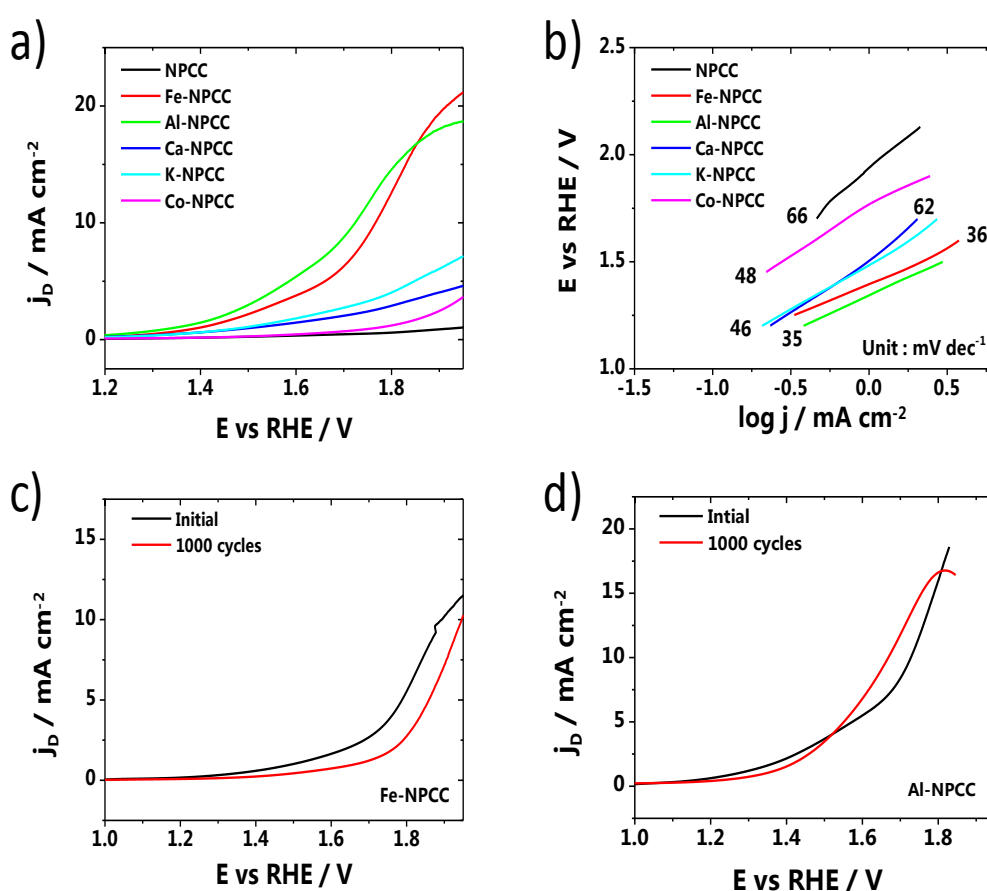


**Figure 6.** a) LSV curves and b) Tafel plots, of NPCC and metal (Fe, Al, Ca, K and Co)-doped NPCC sample electrode in 0.1 M NaOH. Stability test of c) Fe-NPCC and d) Al-NPCC by LSV at a scan rate of  $5 \text{ mV s}^{-1}$  with electrode rotation at 1600 rpm in  $\text{O}_2$ -saturated 0.1 M NaOH before and after 1000 cyclic voltammograms.

The excellent bifunctional ORR/OER activity of the metal-doped NPCC catalysts stimulated us to further examine their practical application as reversible oxygen electrodes for rechargeable Zn–air batteries. We therefore constructed a rechargeable Zn-air battery, which consisted of a Zn-foil as an anode, metal-containing NPCC catalysts loaded on carbon paper as the air electrodes, and 6 M KOH with 0.2 M  $\text{ZnCl}_2$  as the electrolyte. The addition of  $\text{ZnCl}_2$  was to ensure occurrence of a reversible  $\text{Zn}/\text{Zn}^{2+}$  electrochemical redox reaction at the anode <sup>[5,48]</sup>. A green light-emitting diode (LED, 2 V) powered by such two Zn-air batteries in series with the cathode constructed using Fe-NPCC and Al-NPCC catalysts sustained bright light for more than 80 h (Figure 7a, 7b and Figure S6) , underlining the robustness of the developed catalysts. Moreover, the constructed batteries also showed outstanding rechargeability and cycle durability. Galvanostatic charging and discharging tests at a current density of  $5 \text{ mA cm}^{-2}$  (Figure 7c, 7d and Figure S6) revealed that the voltage difference between the charging and discharging processes remained constant over 84 hours (500 cycles with 600 s for each cycle). This confirms excellent bifunctional capability of the batteries, in accordance with the results from the half-reaction tests. The voltage difference of the Al-NPCC containing battery increased slightly during the cycling process, which is attributed to partial dissolution of unstable metals as aluminates ( $\text{Al}(\text{OH})_4^-$ ) into the electrolyte and detachment of loosely attached amorphous carbon. After this initial deactivation process, the voltage difference between the charging and discharging process

was then maintained through the 500<sup>th</sup> cycle with  $\Delta E$  being only as low as 0.62 V. The steady voltage difference between the charging and discharging voltages of Fe-NPCC, Ca-NPCC, K-NPCC, and Co-NPCC after 500 test cycles were 0.73, 0.76, 0.78, and 0.78 V, respectively. Although the incorporated trace metals might partially dissolve into the alkaline solution with time, the formed porous carbon structure with defects coincidentally enhances the performance of oxygen reaction, thereby ensuring long-term stability [49-52]. This superior rechargeability of the batteries fabricated in this study unequivocally demonstrates the potential application of coal derived carbon catalysts incorporated with trace metals in building Zn-air batteries.

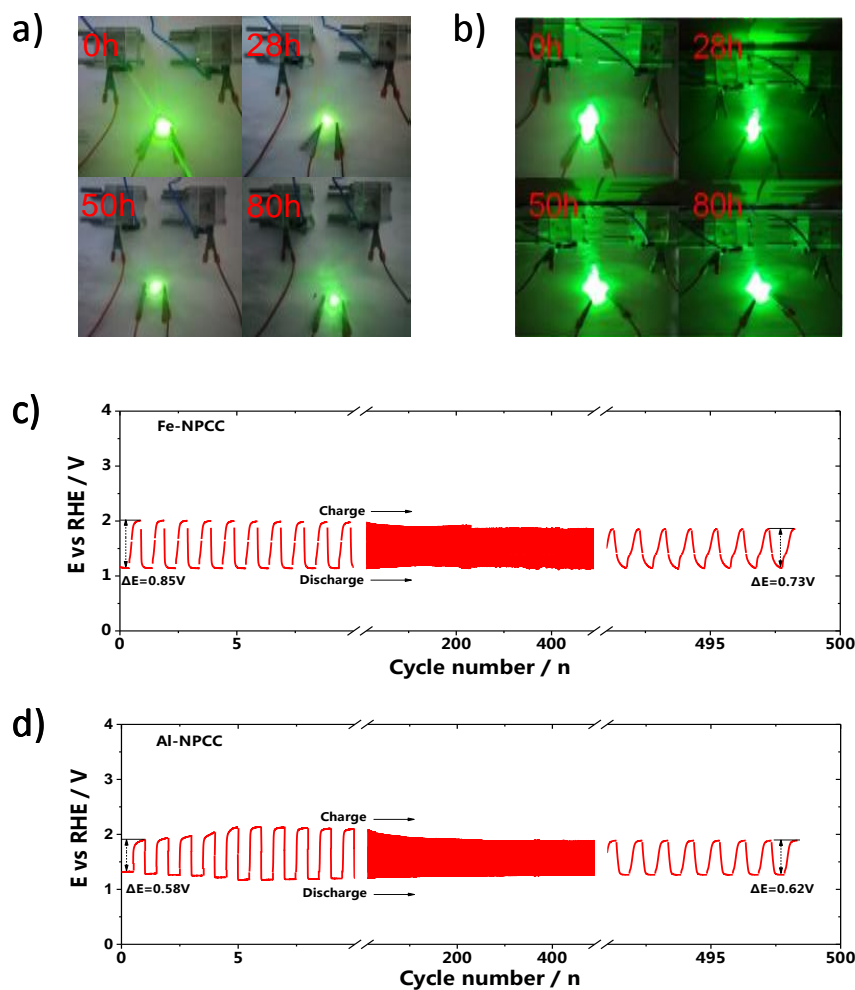


**Figure 7.** a) Photo of a green LED bulb powered by the assembled Zn–air batteries using a) Fe-NPCC and b) Al-NPCC as the cathode and Zinc-foil as anode, and the performance of rechargeable Zn-air batteries based on c) Fe-NPCC and d) Al-NPCC as the cathode and Zinc-foil as anode at a current density of  $5 \text{ mA cm}^{-2}$  in galvanostatic charging/discharging cycles.

### 3. Conclusion

To summarize, we made a systematic study the role of various trace metals on the performance of N-doped coal-derived carbon (NPCC) materials as bifunctional ORR/OER electrocatalysts for rechargeable metal-air batteries. We found that modification of purified coal-derived carbon doped with nitrogen

(NPCC) with trace amounts (1 wt.%) of Fe, Al, Ca, K, and Co can significantly enhance the ORR. Among the investigated catalysts, NPCC modified with traces of Fe, Al, and Ca delivered the best ORR activity, and the obtained catalysts maintained stable ORR performance at  $-1 \text{ mA cm}^{-2}$  for 280 h, and also exhibited excellent resistance against methanol resistance, much better than Pt/C. Both Fe- and Al-containing NPCC catalysts, that is Al-NPCC and Fe-NPCC, also presented good OER performance with excellent stability. Moreover, the as-prepared NPCC samples with trace metals also exhibited very promising potential as durable air electrode catalysts for rechargeable metal-air batteries. Green LED bulbs powered by two custom-made Zn-air cells connected in series maintained bright light for more than 80 h. Charge-discharge tests revealed impressive rechargeability and cycle durability of the constructed Zn-air batteries. This work thus uncovers the possibility of converting source-abundant coal into highly promising electrocatalysts for energy applications especially in rechargeable metal-air batteries.

## Acknowledgement

Financial support from National Natural Science Foundation of China (21605067, 21763023), The Talent Project Grant of the University of Science and Technology Liaoning (601011507-06), and The Doctoral Start-up Research Funding of the University of Science and Technology Liaoning (USTL010178), China are acknowledged.

## References

- [1] W. R. Cheng, X. Zhao, H. Su, F. M. Tang, W. Che, H. Zhang, etc., Lattice-strained metal-organic-framework arrays for bifunctional oxygen electrocatalysis, *Nat. Energy*. 4 (2019) 115-122.
- [2] J. J. Bana, G. C. Xua, L. Zhang, G. Xua, Li. J. Yang, Z. P. Sun, etc., Efficient Co-N/PC@CNT bifunctional electrocatalytic materials for oxygen reduction and oxygen evolution reactions based on metal-organic framework, *Nanoscale* 10 (2018) 9077-9086.
- [3] V. R. Stamenkovic, D. Strmcnik, P. P. Lopes, N. M. Markovic, Energy and fuels from electrochemical interfaces, *Nat. Mater.* 16(2017) 57-69.
- [4] N. T. Suen, S. F. Hung, Q. Quan, N. Zhang, Y. J. Xu, H. M. Chen, Electrocatalysis for the oxygen evolution reaction: recent development and future perspectives, *Chem. Soc. Rev.* 46 (2017) 337-365.
- [5] Q. C. Wang, Y. P. Lei, Z. Y. Chen, N. Wu, Y. B. Wang, B. Wang, etc., Fe/Fe<sub>3</sub>C@C nanoparticles encapsulated in N-doped graphene-CNTs framework as an efficient bifunctional oxygen electrocatalyst for robust rechargeable Zn-air batteries, *J. Mater. Chem. A*. 6 (2018) 516-526.
- [6] Y. B. Guo, Y. N. Chen, H. J. Cui, Z. Z. NiCo<sub>2</sub>S<sub>4</sub> nanocrystals anchored on nitrogen-doped carbon nanotubes as a highly efficient bifunctional electrocatalyst for rechargeable zinc-air batteries, *Nano Energy*. 31 (2017) 541-550.
- [7] Z. K. Yang, Y. Wang, M. Z. Zhu, Z. J. Li, W. X. Chen, W. C. Wei, etc., Boosting oxygen reduction catalysis with Fe-N<sub>4</sub> sites decorated porous carbons towards fuel

cells, *ACS Catal.* 9 (2019) 2158-2163.

[8] Y. Gorlin, T. F. Jaramillo, A bifunctional nonprecious metal catalyst for oxygen reduction and water oxidation, *J. Am. Chem. Soc.* 132 (2010) 13612-13614.

[9] A. Majeed, P. X. Hou, F. Zhang, H. Tabassum, X. Li, G. X. Li, etc., A freestanding single-wall carbon nanotube film decorated with N-doped carbon-encapsulated Ni Nanoparticles as a bifunctional electrocatalyst for overall water splitting, *Adv. Sci.* 6 (2019) 1802177.

[10] Y. J. Zhang, C. Wang, N. F. Wan, Z. Q. Mao, Deposited  $\text{RuO}_2\text{-IrO}_2/\text{Pt}$  electrocatalyst for the regenerative fuel cell, *Int. J. Hydrogen. Energy.* 32 (2007) 400-404.

[11] X. X. Chen, J. Wang, X. N. Huang, X. F. Zhao, P. G. Liu, B. C. He, etc., Simple conversion of earth-abundant coal to high-performance bifunctional catalysts for reversible oxygen electrodes, *Catal. Sci. Technol.* 8 (2018) 1104-1112.

[12] A. P. Tiwari, D. Kim, Y. Kim, H. Lee, Bifunctional oxygen electrocatalysis through chemical bonding of transition metal chalcogenides on conductive carbons, *Adv. Energy Mater.* 7 (2017) 1602217-1602225.

[13] B. C. He, X. X. Chen, J. M. Lu, S. D. Yao, J. Wei, Q. Zhao, etc., One-pot synthesized  $\text{Co}/\text{Co}_3\text{O}_4\text{-N-graphene}$  composite as electrocatalyst for oxygen reduction reaction and oxygen evolution reaction, *Electroanal.* 28 (2016) 2435-2444.

[14] F. Razmjooei, K. P. Singh, D. S. Yang, W. Cui, Y. H. Jang, J. S. Yu, Fe-treated heteroatom (S/N/B/P)-doped graphene electrocatalysts for water oxidation, *ACS Catal.* 7 (2017) 2381-2391.

- [15] J. C. Li, X. P. Qin, P. X. Hou, M. Cheng, C. Shi, C. Liu, etc., Identification of active sites in nitrogen and sulfur co-doped carbon-based oxygen reduction catalysts, *Carbon* 147 (2019) 303-311.
- [16] R. Wu, S. G. Chen, Y. L. Zhang, Y. Wang, W. Ding, L. Li, etc., Template-free synthesis of hollow nitrogen-doped carbon as efficient electrocatalysts for oxygen reduction reaction, *J. Power Sources*. 274 (2015) 645-650.
- [17] J. Wu, C. Jin, Z. R. Yang, J. H. Tian, R. Z. Yang, Synthesis of phosphorus-doped carbon hollow spheres as efficient metal-free electrocatalysts for oxygen reduction, *Carbon* 82 (2015) 562-571.
- [18] J. C. Li, Z. Q. Yang, D. M. Tang, L. Zhang, P. X. Hou, S. Y. Zhao, etc., N-doped carbon nanotubes containing a high concentration of single iron atoms for efficient oxygen reduction, *NPG Asia Mater.* 10 (2018) e461.
- [19] Z. J. Lu, X. X. Chen, P. G. Liu, X. N. Huang, J. Wei, Z. Ren, etc., Co-Mn hybrid oxides supported on N-doped graphene as efficient electrocatalysts for reversible oxygen electrodes, *J. Electrochem. Soc.* 165 (2018) H580-H589.
- [20] S. M. Shamsunnahar, M. Nagai, Nitrogen doping of ash-free coal and effect of ash components on properties and oxygen reduction reaction in fuel cell, *Fuel* 126 (2014) 134-142.
- [21] M. Muraoka, H. Tominaga, M. Nagai, Iron addition to Vietnam anthracite coal and its nitrogen doping as a PEFC non-platinum cathode catalyst, *Fuel* 102 (2012) 359-365.

- [22] M. Muraoka, M. Nagai, Coals as a novel cathode catalyst for polymer electrolyte fuel cell, *Fuel* 94 (2012) 204-210.
- [23] M. Muraoka, H. Tomonaga, M. Nagai, Ammonia-treated brown coal and its activity for oxygen reduction reaction in polymer electrolyte fuel cell, *Fuel* 97 (2012) 211-218.
- [24] X. X. Chen, X. N. Huang, T. Wang, S. Barwe, K. P. Xie, Y. U. Kayran, etc., Traditional earth-abundant coal as new energy materials to catalyze the oxygen reduction reaction in alkaline solution, *Electrochim. Acta* 211 (2016) 568-575.
- [25] H. R. Pan, D. L. Wu, X. N. Huang, K. P. Xie, B. C. He, Z. J. Lu, etc., Microwave-assisted synthesis of Co/CoO<sub>x</sub> supported on earth-abundant coal-derived carbon for electrocatalysis of oxygen evolution, *J. Electrochem. Soc.* 166 (2019) F479-F486.
- [26] H. M. Liu, J. X. Cheng, Z. J. Lu, X. N. Huang, Y. M. Zhu, X. F. Zhao, etc., Significant enhancement of the oxygen reduction activity of self-heteroatom doped coal derived carbon through oxidative pretreatment, *Electrochim. Acta* 312 (2019) 22-30.
- [27] J. T. Zhu, J. C. Jia, F. L. Kwong, D. H. L. Ng, P. A. Crozier, Metal-free synthesis of carbon nanotubes filled with calcium silicate, *Carbon* 50 (2012) 2666-2674.
- [28] T. H. R. da Cunha, S. de Oliveira, I. L. Martins, V. Geraldo, D. Miquita, S. L. M. Ramos, etc., High-yield synthesis of bundles of double- and triple-walled carbon nanotubes on aluminum flakes, *Carbon* 133 (2018) 53-61.
- [29] A. Roussey, N. Venier, H. Fneich, L. Giardella, T. Pinaud, S. Tahir, etc., One-pot preparation of iron/alumina catalyst for the efficient growth of vertically-aligned carbon nanotube forests, *Mater. Sci. Eng. B.* 245 (2019) 37-46.
- [30] A. Y. S. Eng, H. L. Poh, J. Luxa, Z. Sofer, M. Pumera, Potassium assisted reduction

and doping of graphene oxides: towards faster electron transfer kinetics, *RSC Adv.* 3 (2013) 10900-10908.

[31] J. F. Wang, L. J. Jin, Y. Zhou, Y. Li, H. Q. Hu, Effect of  $\text{Ca}(\text{NO}_3)_2$  addition in coal on properties of activated carbon for methane decomposition to hydrogen, *Fuel Process. Technol.* 176 (2018) 85-90.

[32] X. X. Chen, N. Li, K. Eckhard, L. Stoica, W. Xia, J. Assmann, etc., Pulsed electrodeposition of Pt nanoclusters on carbon nanotubes modified carbon materials using diffusion restricting viscous electrolytes, *Electrochem. Commun.* 9 (2007) 1348-1354.

[33] Y. P. Li, J. Y. Gao, F. Zhang, Q. Z. Qian, Y. Liu, G. Q. Zhang, Hierarchical 3D macrosheets composed of interconnected in-situ cobalt catalyzed nitrogen doped carbon nanotubes as superior bifunctional oxygen electrocatalysts for rechargeable Zn-air batteries, *J. Mater. Chem. A.* 6 (2018) 15523-15529.

[34] C. T. Chong, W. H. Tan, S. L. Lee, W. W. F. Chong, S. S. Lam, A. Valera-Medina, Morphology and growth of carbon nanotubes catalytically synthesized by premixed hydrocarbon-rich flames, *Mater. Chem. Phys.* 197 (2017) 246-255.

[35] T. Wang, L. X. Wang, D. L. Wu, W. Xia, D. Z. Jia, Interaction between nitrogen and sulfur in co-doped graphene and synergetic effect in supercapacitor, *Sci. Rep.* 5 (2015) 9591-9599.

[36] H. P. Cong, P. Wang, M. Gong, S. H. Yu, Facile synthesis of mesoporous nitrogen-doped grapheme: an efficient methanol-tolerant cathodic catalyst for oxygen reduction reaction, *Nano Energy* 3 (2014) 55-63.

- [37] Z. G. Wang, P. J. Li, Y. F. Chen, J. B. Liu, H. J. Tian, J. H. Zhou, etc., Synthesis of nitrogen-doped graphene by chemical vapour deposition using melamine as the sole solid source of carbon and nitrogen, *J. Mater. Chem. C*. 2 (2014) 7396-7401.
- [38] S. Kundu, Y. M. Wang, W. Xia, M. Muhler, Thermal stability and reducibility of oxygen-containing functional groups on multiwalled carbon nanotube surfaces: a quantitative high-resolution XPS and TPD/TPR study, *J. Phys. Chem.* 112 (2008) 16869-16878.
- [39] J. Liu, X. J. Sun, P. Song, Y. W. Zhang, W. Xing, W. L. Xu, High-performance oxygen reduction electrocatalysts based on cheap carbon black, nitrogen and trace iron, *Adv. Mater.* 25 (2013) 6879-6883.
- [40] M. A. Pimenta, G. Dresselhaus, M. S. Dresselhaus, L. G. Cancado, A. Jorio, R. Saito, Studying disorder in graphite-based systems by Raman spectroscopy, *Phys. Chem. Chem.* 9 (2007) 1276-1290.
- [41] A. C. Ferrari, Raman spectroscopy of graphene and graphite: disorder, electron–phonon coupling, doping and nonadiabatic effects, *Solid. State. Commun.* 143 (2007) 47-57.
- [42] X. Sun, X. Wang, N. Feng, L. Qiao, X. Li, D. He, A new carbonaceous material derived from biomass source peels as an improved anode for lithium ion batteries, *J. Anal. Appl. Pyrolysis*. 100 (2013) 181-185.
- [43] J. T. Klopogge, B. J. Wood, Systematic XPS study of gallium-substituted boehmite, *J. Mater. Sci.* 51 (2016) 5436-5444.
- [44] M. D. McKee, J. R. Martin, W. J. Landis, Biophysical analyses of sequential bands

of enamel related to ruffle-ended and smooth-ended maturation ameloblasts, *J. Dent. Res.* 68 (1989) 101-106.

[45] R. J. Toh, H. L. Poh, Z. Sofer, M. Pumera, Transition metal (Mn, Fe, Co, Ni)-doped graphene hybrids for electrocatalysis, *Chem. Asian. J.* 8 (2013) 1295-1300.

[46] R. R. Liu, H. M. Zhang, S. W. Liu, X. Zhang, T. X. Wu, X. Ge, etc., Shrimp-shell derived carbon nanodots as carbon and nitrogen source to fabricate three-dimensional N-doped porous carbon electrocatalyst for oxygen reduction reaction, *Phys. Chem. Chem. Phys.* 18 (2016) 4095-4101.

[47] J. Masa, W. Xia, I. Sinev, A. Q. Zhao, Z. Y. Sun, S. Gruetzke, etc.,  $\text{Mn}_x\text{O}_y/\text{NC}$  and  $\text{Co}_x\text{O}_y/\text{NC}$  nanoparticles embedded in a nitrogen-doped carbon matrix for high-performance bifunctional oxygen electrodes, *Angew. Chem. Int. Ed.* 53 (2014) 8508-8512.

[48] J. Pan, Y. Y. Xu, H. Yang, Z. H. Dong, H. F. Liu, B. Y. Xia, Advanced architectures and relatives of air electrodes in Zn–air batteries, *Adv. Sci.* 5 (2018) 1700691-1700720.

[49] D. F. Yan, Y. X. Li, J. Huo, R. Chen, L. M. Dai, S. Y. Wang, Defect chemistry of nonprecious-metal electrocatalysts for oxygen reactions, *Adv. Mater.* 29 (2017) 1606459.

[50] G. L. Tian, M. Q. Zhao, D. Yu, X. Y. Kong, J. Q. Huang, Q. Zhang, etc., Nitrogen-doped graphene/carbon nanotube hybrids: in situ formation on bifunctional catalysts and their superior electrocatalytic activity for oxygen evolution/reduction reaction, *Small* 10 (2014) 2251-2259.

[51] Y. Jia, L. Zhang, A. Du, G. Gao, J. Chen, X. Yan, etc., Defect graphene as a

trifunctional catalyst for electrochemical reactions, *Adv. Mater.* 28 (2016) 9532-9538.

[52] H. C. Tao, Y. N. Gao, N. Talreja, F. Guo, J. Texter, C. Yan, etc., Two-dimensional nanosheets for electrocatalysis in energy generation and conversion, *J. Mater. Chem. A* 5 (2017) 7257-7284.

## Trace Metals Dramatically Boost Oxygen Electrocatalysis of N-doped Coal-derived Carbon for Zinc-air Battery

Huimin Liu<sup>a</sup>, Xinning Huang<sup>b</sup>, Zhenjie Lu<sup>a</sup>, Tao Wang<sup>c</sup>, Yaming Zhu<sup>a</sup>, Junxia Cheng<sup>a</sup>, Yue Wang<sup>a</sup>, Dongling Wu<sup>c,\*</sup>, Zhenyu Sun<sup>d,\*</sup> and Xingxing Chen<sup>a,\*</sup>

<sup>a</sup> *Research Group of Functional Materials for Electrochemical Energy Conversion, School of Chemical Engineering, University of Science and Technology Liaoning, Qianshan Middle Road 185, 114051 Anshan, P. R. China*

<sup>b</sup> *Engineering Training Center, University of Science and Technology Liaoning, Qianshan Road 185, 114051 Anshan, P. R. China*

<sup>c</sup> *Key Laboratory of Energy Materials Chemistry, Institute of Applied Chemistry, Xinjiang University, Shengli Road 14, 830046 Urumqi, P. R. China*

<sup>d</sup> *State Key Laboratory of Organic-Inorganic Composites, College of Chemical Engineering, Beijing University of Chemical Technology, Beijing 100029, P. R. China*

\* *Corresponding authors. E-mail: xingchenstar79@163.com (X. X. Chen), wudl@xju.edu.cn (D. L. Wu), sunzy@mail.buct.edu.cn (Z. Y. Sun)*

## Experimental

### *Chemicals and solutions*

Brown coal was obtained from Hailar Coal Mine, Inner Mongolia, China. Its proximate analysis and EDX analysis can be found in Table S1 and Figure S1<sup>[11]</sup>. NaOH ( $\geq 96\%$ ), HF ( $\geq 40.0\%$ ), HCl (35%), ZnCl<sub>2</sub> (98%), ethanol ( $\geq 99.8\%$ ), and KNO<sub>3</sub> (analytical reagent, AR) were purchased from Tianjin Rgent® Chemicals Co. Ltd. (China). Nafion (5%) and Pt/C (20 wt%) were bought from Sigma-Aldrich (China). FeCl<sub>3</sub>·6H<sub>2</sub>O (AR) was bought from Sinopharm Chemical Reagent Co. Ltd. (China). SiCl<sub>4</sub> (98%), C<sub>4</sub>H<sub>6</sub>CuO<sub>4</sub>·H<sub>2</sub>O (99.0%), AlCl<sub>3</sub> (99%), ethanol (99.5%) were purchased from Shanghai Macklin Biochemical Co. Ltd. (China), KOH ( $\geq 95\%$ ), Co(NO<sub>3</sub>)<sub>2</sub>·6H<sub>2</sub>O (ACS), NiN<sub>2</sub>O<sub>6</sub>·6H<sub>2</sub>O (98%), MgCl<sub>2</sub> (99.9%), and CaCl<sub>2</sub> ( $>96\%$ ) were obtained from Aladdin Reagent Co. Ltd. (China). C<sub>4</sub>H<sub>6</sub>MnO<sub>4</sub>·4H<sub>2</sub>O (99.0% ) was supplied from Tianjin Damao Chemical Reagent Factory. All aqueous solutions were prepared using triple-distilled deionized water.

### *Sample preparation*

The original brown coal (OC) was first crushed by ball milling followed by drying in an oven at 378 K for 4 h to obtain air-dried coal. 7.0 g of the crushed coal was then added to 140 mL of triple-distilled deionized water and left at room temperature for 12 h with continuous stirring of the solution. The suspension was filtered and washed with water. To 6 g of the washed coal was added to 36 mL of 5.4 M HCl. The suspension was continuously stirred for 24 h at room temperature, afterwards, the sample was filtered and washed with water until no  $\text{Cl}^-$  was measurable in the waste solution detected by adding a drop of  $\text{AgNO}_3$  to observe the formation of AgCl precipitation. To 5 g of the HCl-washed coal was added 40 mL of HF solution (40 wt%) and stirred at room temperature for 24 h. The purified coal (PC) was finally obtained after filtration and further washed with water until the solution reached a pH of 7. PC was then added to different trace element precursors ( $\text{FeCl}_3 \cdot 6\text{H}_2\text{O}$ ,  $\text{AlCl}_3$ ,  $\text{CaCl}_2$ ,  $\text{KNO}_3$ ,  $\text{Co}(\text{NO}_3)_2 \cdot 6\text{H}_2\text{O}$ ,  $\text{SiCl}_4$ ,  $\text{MgCl}_2$ ,  $\text{C}_4\text{H}_6\text{CuO}_4 \cdot \text{H}_2\text{O}$ ,  $\text{NiN}_2\text{O}_6 \cdot 6\text{H}_2\text{O}$ , or  $\text{C}_4\text{H}_6\text{MnO}_4 \cdot 4\text{H}_2\text{O}$ ) in an ethanol solution. The trace element (Fe, Al, Ca, K, Co, Si, Mg, Cu, Ni, or Mn) to PC weight ratio was 1 wt%, respectively. After thorough mixing of the suspension, it was dried at room temperature overnight. The samples were individually put in a quartz boat and inserted into a chemical vapor deposition (CVD) reactor. The reactor was first flushed with Ar at room temperature for 15 min to remove air, and then heated in a stream of  $\text{NH}_3$  and Ar (1:9 volume ratio) at a flow rate of  $100 \text{ mL min}^{-1}$  to  $1050^\circ\text{C}$  at a heating rate

of  $10\text{ }^{\circ}\text{C min}^{-1}$ . The reactor was then held at this temperature for 2 h and cooled down in the same  $\text{NH}_3/\text{Ar}$  atmosphere at a flow rate of  $100\text{ mL min}^{-1}$  to room temperature. The prepared catalysts are denoted as NPCC (N-doped purified coal-derived carbon), without the addition of trace elements, as the reference sample, Fe-NPCC, Al-NPCC, Ca-NPCC, K-NPCC, Co-NPCC, Si-NPCC, Mg-NPCC, Cu-NPCC, Ni-NPCC, and Mn-NPCC.

### *Electrochemical measurements*

The electrochemical performance of the prepared catalysts was evaluated using a bipotentiostat (CHI 760E, CH Instruments, China) in combination with a speed-control unit (PINE Research Instrumentation, USA). 1 mL of the sample suspension containing 5 mg of the catalyst powder, 20  $\mu\text{L}$  Nafion (5%), 490  $\mu\text{L}$  ethanol, and 490  $\mu\text{L}$  water was prepared with the aid of ultrasonication for 30 min. A rotating ring disk electrode (RRDE) with glassy carbon ( $A = 0.2472\text{ cm}^2$ ) as the disk and Pt ( $A = 0.1866\text{ cm}^2$ ) as the ring, and a glassy carbon rotating disk electrode (RDE) ( $A = 0.196\text{ cm}^2$ ) served as the working electrode on which the catalyst ink (10.4  $\mu\text{L}$  for the RRDE or 8.3  $\mu\text{L}$  for the RDE) were drop coated to get a final catalyst loading of  $0.21\text{ mg cm}^{-2}$ . A Ag/AgCl/3M KCl electrode and a glassy carbon plate were used as reference electrode and counter electrode, respectively. Before each measurement, the electrodes were polished on a polishing cloth using  $\text{Al}_2\text{O}_3$  paste of 0.3  $\mu\text{m}$  grain size followed by rinsing with triple-distilled deionized water. The electrode was first electrochemically preconditioned in Ar-saturated 0.1 M NaOH by running cyclic

voltammetry (CV) in the potential range of 0 to -1 V vs. Ag/AgCl/3M KCl at a scan rate of 100 mV s<sup>-1</sup> until reproducible voltammograms were obtained (typically 20 cycles). Linear sweep voltammetry (LSV) measurements were carried out in the same electrolyte saturated, first with Ar to record the background current, then with O<sub>2</sub> within the same potential window at a rotation speed of 1600 rpm to record the performance of the catalysts for ORR. During the ORR activity measurements, the Pt-ring of RRDE was meanwhile held at a fixed potential of 0.4 V to study H<sub>2</sub>O<sub>2</sub> production during ORR. To evaluate the OER performance of the catalysts, LSV was carried out between 0 to 1.2 V vs. Ag/AgCl/3M KCl at a scan rate of 5 mV s<sup>-1</sup> in O<sub>2</sub>-saturated 0.1 M NaOH with a rotating speed of 1600 rpm. Kinetic analysis of the ORR was performed by Koutecky Levich (K-L) analysis using the equation given below <sup>[11]</sup>:

$$1/j = 1/j_L + 1/j_K = 1/B\omega^{1/2} + 1/j_K$$

$$B = 0.62nFC_0D^{2/3}V^{-1/6}$$

$$j_K = nFkC_0$$

where  $j$  is the measured current density at the glassy carbon,  $j_K$  and  $j_L$  are the kinetic and diffusion-limiting current densities, respectively,  $\omega$  is the angular velocity of the electrode,  $B$  is the Levich slope,  $n$  is the number of electrons transferred in the ORR process,  $F$  is the Faraday constant (96485 C mol<sup>-1</sup>),  $D$  is the diffusion coefficient of dissolved oxygen in the electrolyte, which for a 0.1 M NaOH solution is 1.90x10<sup>-5</sup> cm<sup>2</sup> s<sup>-1</sup>, and  $C_0$  is the concentration of oxygen in

the electrolyte ( $1.2 \times 10^{-6} \text{ mol cm}^{-3}$ ),  $\nu$  is the kinematic viscosity of the electrolyte ( $0.01 \text{ cm}^2 \text{ s}^{-1}$ ), and  $k$  is the rate constant for the ORR ( $\text{m s}^{-1}$ ).

The yield of the intermediate product (%  $\text{HO}_2^-$ ) and the number of transferred electrons ( $n$ ) during the ORR were calculated from the RRDE data using the following two equations <sup>[11]</sup>:

$$\text{HO}_2^- (\%) = 200 * \{(I_R / N_0) / [(I_R/N_0) + I_D]\}$$

$$n = 4 * I_D / [(I_R/N_0) + I_D]$$

where  $I_D$  is the disk current,  $I_R$  is the ring current, and  $N_0$  is the collection efficiency of the ring electrode (0.37) (Pine Research Instrumentation, USA).

The long-term stability of the catalysts for the ORR was tested by applying a constant current density at  $-1 \text{ mA cm}^{-2}$  for 280 h in  $\text{O}_2$ -saturated 0.1 M NaOH. Methanol poisoning experiments were carried out to check the effect of methanol crossover by addition of 3 M methanol (1% v/v) into the electrolyte under magnetic stirring while the electrode was poised at a constant potential of  $-0.2 \text{ V}$ . For the OER, the stability of the catalysts was evaluated by running cyclic voltammograms in the potential range of 0 to 1.2 V at a scan rate of  $100 \text{ mV s}^{-1}$  for 1000 cycles and recording the linear sweep voltammograms at a scan rate of  $5 \text{ mV s}^{-1}$  before and after the 1000 CV cycles.

The potentials reported in the experimental description are with respect to the Ag/AgCl/3 M KCl reference electrode, while all the potentials reported in the following results were corrected for the resistance of the solution ( $iR_s$ ) and converted to the reversible hydrogen electrode (RHE) by the equation <sup>[11]</sup>:

$$E = E_{\text{Ag/AgCl}} + E^0_{\text{Ag/AgCl}} + 0.059 \cdot \text{pH} - iR_s$$

where  $E$  is potential versus RHE,  $E_{\text{Ag/AgCl}}$  is the measured potential vs. Ag/AgCl/3M KCl,  $E^0_{\text{Ag/AgCl}}$  is the standard potential of the Ag/AgCl/3M KCl at zero pH (0.207 V) on the standard hydrogen electrode (SHE) scale,  $R_s$  is the resistance of the electrolyte. Rechargeable Zn–air batteries were assembled by using a zinc-foil as the anode, and the catalyst supported on carbon paper as the air cathode, and 6 M KOH containing 0.2 M  $\text{ZnCl}_2$  as the electrolyte. The catalyst ink was sprayed onto the carbon paper to an average loading of  $1.0 \text{ mg cm}^{-2}$  and dried at room temperature. The charge/discharge performance and cycling stability were measured at an alternating current density of  $5 \text{ mA cm}^{-2}$  with each cycle lasting 600 s for 500 cycles in total.

### *Characterization of samples*

Scanning electron microscopy (SEM, HITACHI SU8010) and high-resolution transmission electron microscopy (TEM, HITACHI H-600) were used to characterize the morphology and structure of the as-produced samples. Raman spectra were recorded using a Bruker Vertex 70 system (532 nm laser). X-ray diffraction (XRD) measurements were carried out on a Bruker D8 X-ray diffractometer in the  $2\theta$  range from 10 to  $80^\circ$ , with a  $\text{Cu K}\alpha$  radiation ( $\lambda = 1.5418 \text{ \AA}$ ) source. X-ray photoelectron spectroscopy (XPS) measurements were carried out using an ESCALab 250Xi electron spectrometer equipped with a 300 W  $\text{Al K}\alpha$  X-ray source. Elemental analysis of C, N, H, S, and O was

performed on an elemental analyzer Vario EL.

**Table S1.** Proximate analysis of coal samples from three different locations of Hailar coal mine.

Sample	M <sub>ad</sub> <sup>[a]</sup> /%	A <sub>ad</sub> <sup>[b]</sup> /%	V <sub>ad</sub> <sup>[d]</sup> /%	V <sub>daf</sub> <sup>[d]</sup> /%	FC <sub>ad</sub> <sup>[e]</sup> /%
Original Coal	30.87	10.30	26.46	---	32.37

<sup>[a]</sup> M<sub>ad</sub>: moisture, <sup>[b]</sup> A<sub>ad</sub>: ash, <sup>[c]</sup> V<sub>ad</sub>: volatile matter, <sup>[d]</sup> V<sub>daf</sub>: volatile matter, <sup>[e]</sup> FC<sub>ad</sub>: fixed carbon (All the quantities are on a dry weight basis).

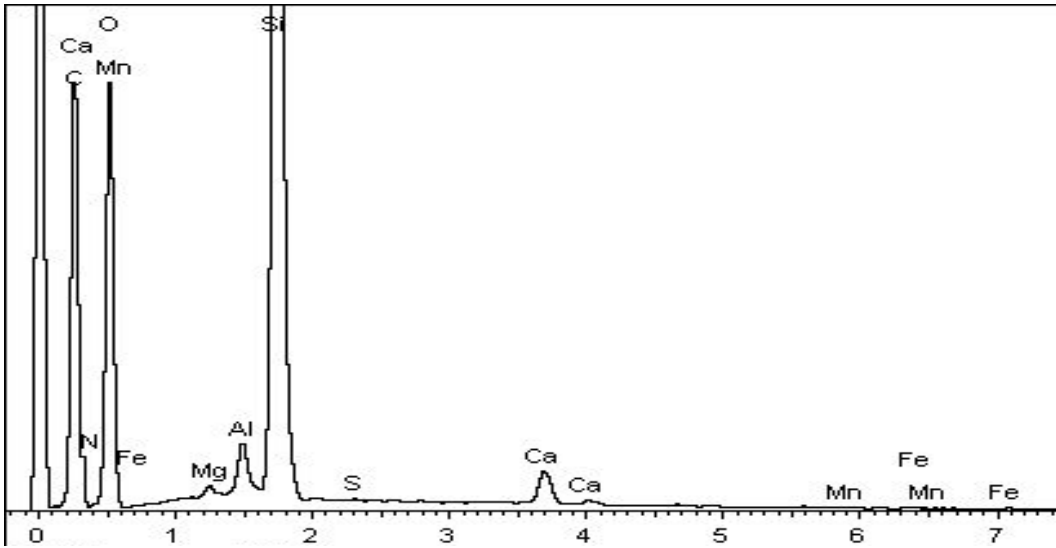


**Figure S1.** EDS spectrum of original coal revealing the presence of trace elements, such as Si, Ca, Mn, Fe, Al and Mg.

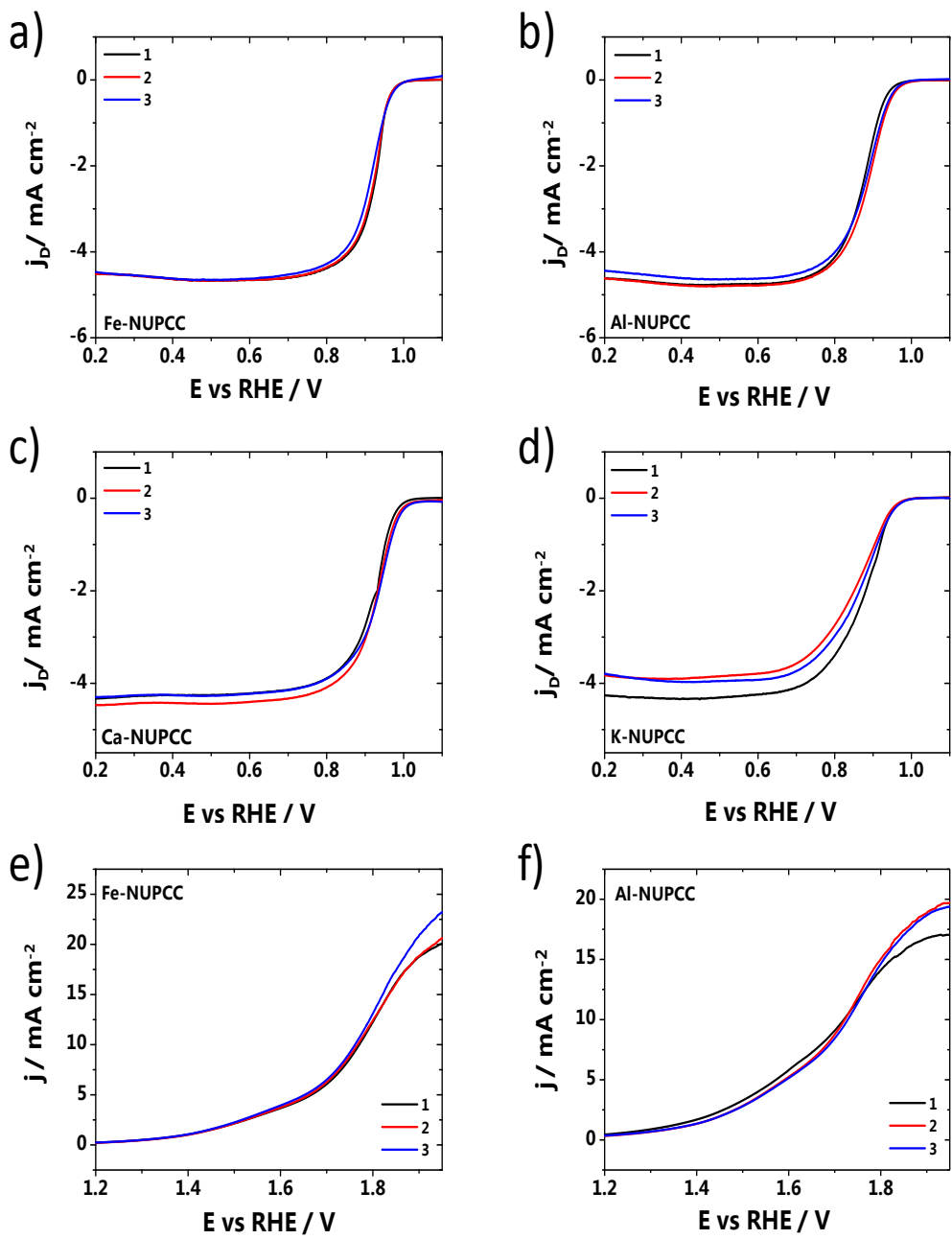


**Figure S2.** Linear sweep voltammograms showing the ORR performance of N-doped coal derived carbon modified with 1% wt. of the respective metals indicated a) Fe-NPCC, b) Al-NPCC, c) Ca-NPCC, d) K-NPCC, and the OER on e) Fe-NPCC and f) Al-NPCC.

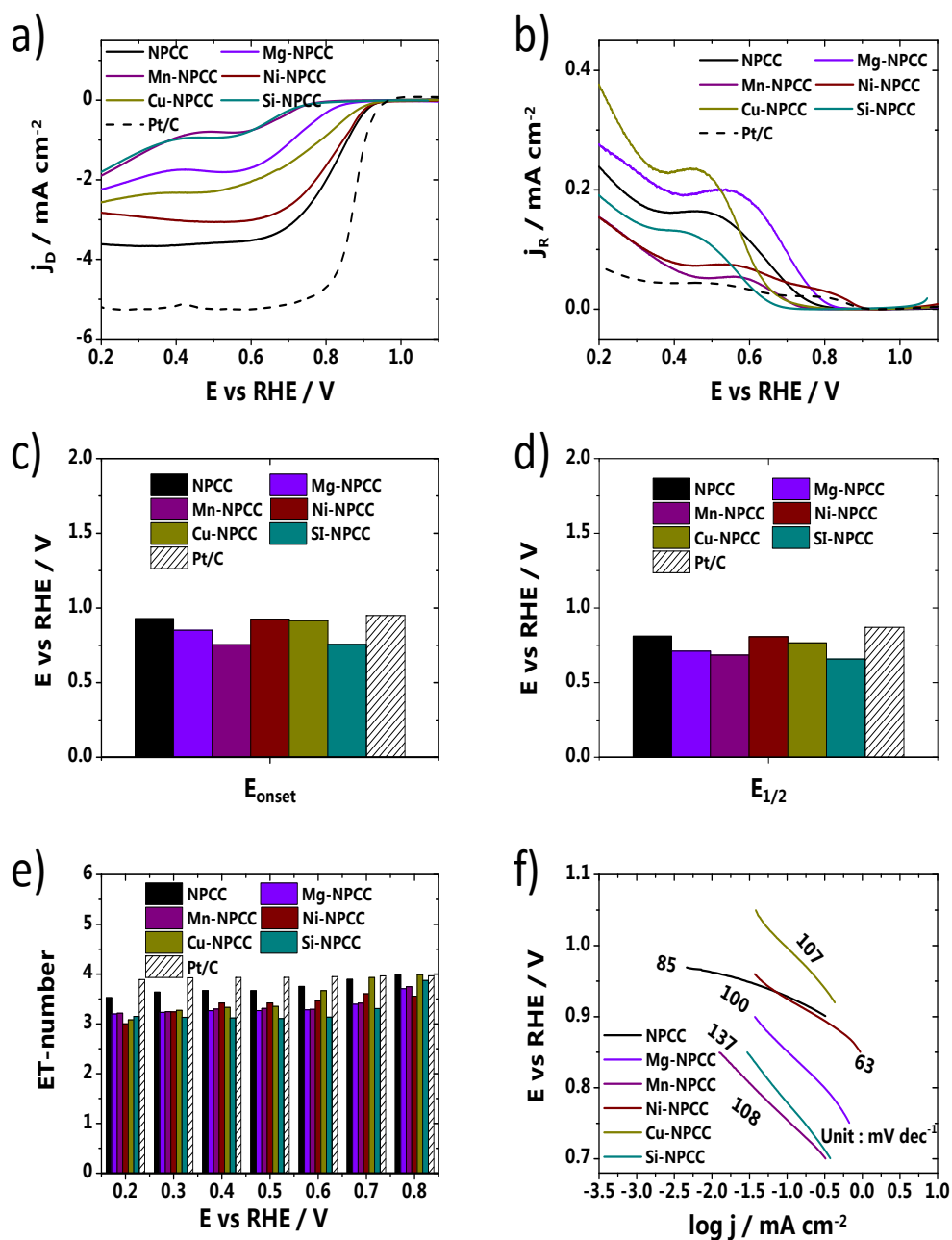


**Figure S3.** a) Linear sweep voltammetry (LSV) curves of NPCC and metal (Mg, Mn, Ni, Cu and Si)-doped NPCC samples showing a) the ORR and b) H<sub>2</sub>O<sub>2</sub> production, measured in O<sub>2</sub>-saturated 0.1 M NaOH solution with a scan rate of 5 mV s<sup>-1</sup> and electrode rotation at 1600 rpm, c) onset potential, d) half-wave potential, e) average electron transfer number at different potentials, f) Tafel plots derived from the ORR curves in a).

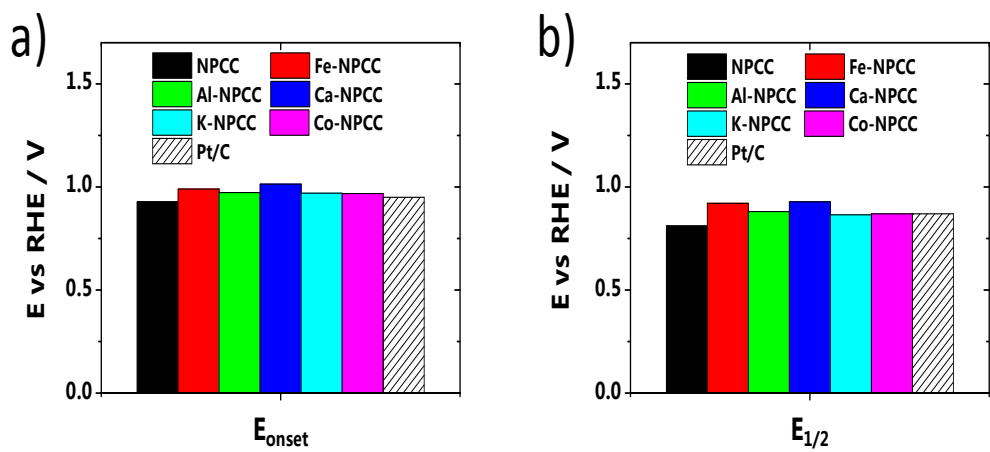


**Figure S4.** a) Onset potential, b) half-wave potential of the NPCC and metal (Fe, Al, Ca, K and Co)-doped NPCC samples during ORR.

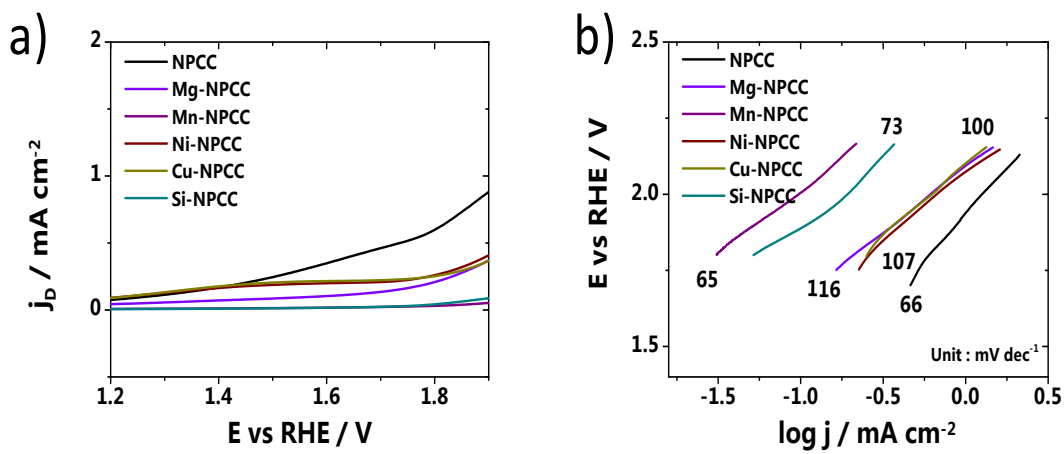


**Figure S5.** a) LSV curves of NPCC and metal (Mg, Mn, Ni, Cu and Si)-doped NPCC sample electrodes showing the OER of the catalysts in 0.1 M NaOH, (b) corresponding Tafel plots.

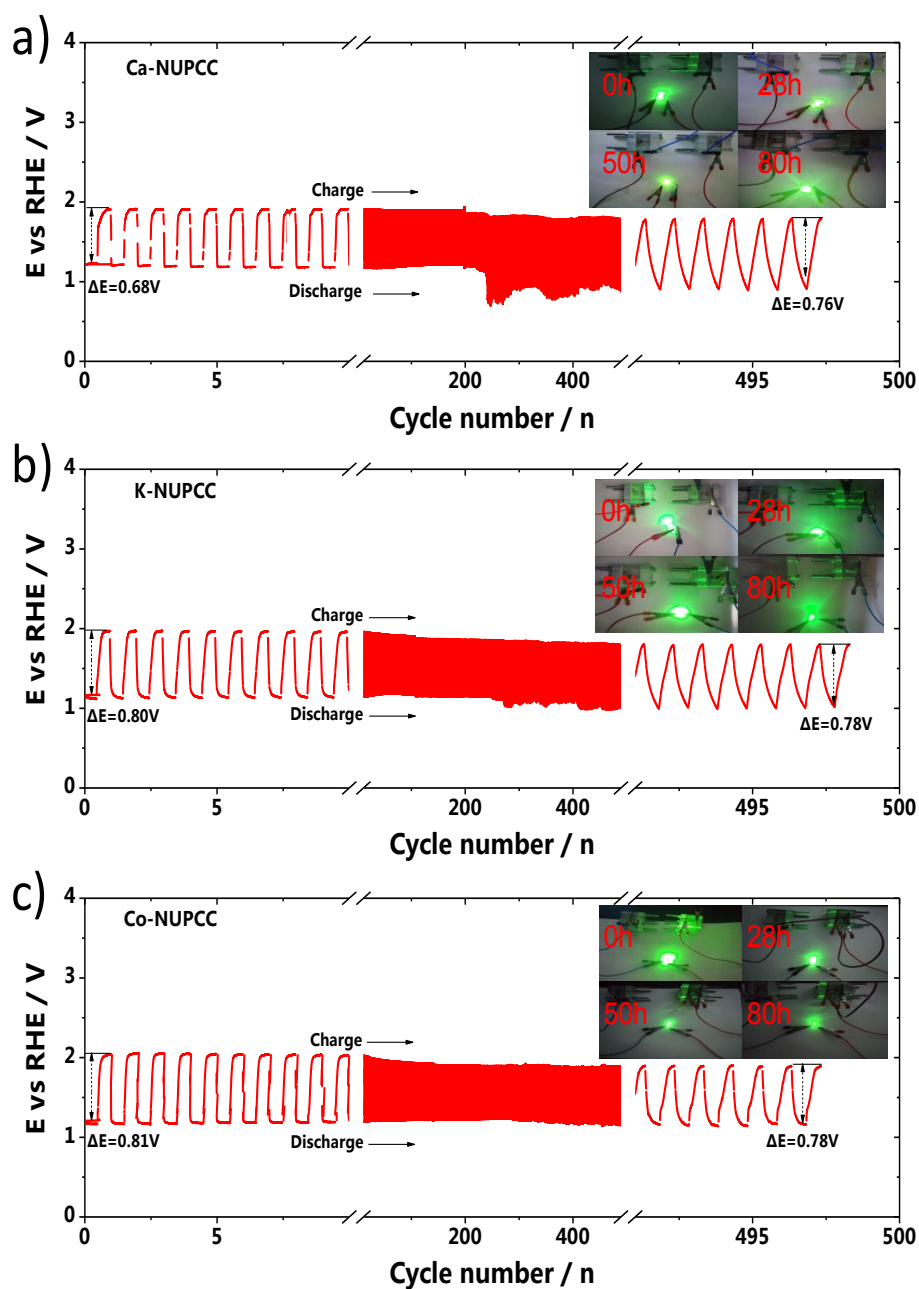


**Figure S6.** Photos of green LED bulbs powered by the assembled Zn–air batteries, and the performance of rechargeable Zn–air batteries based on a) Ca-NUPCC b) K-NUPCC and c) Co-NUPCC as the cathode and Zinc-foil as anode at a current density of 5 mA cm<sup>-2</sup> in galvanostatic charging/discharging cycles.